



# Geotechnical Testing Journal

---

Qi Luo,<sup>1</sup> Dan Zhang,<sup>2</sup> Hasanjan Yimit,<sup>1</sup> Jingwen Su,<sup>3</sup> Haoyu Wang,<sup>1</sup> and Haiyang Liao<sup>1</sup>

**DOI: 10.1520/GTJ20230370**

Effects of Cable Sheath on  
Deformation Coordination  
between the Sensing Fiber  
and Sand

---

Qi Luo,<sup>1</sup> Dan Zhang,<sup>2</sup> Hasanjan Yimit,<sup>1</sup> Jingwen Su,<sup>3</sup> Haoyu Wang,<sup>1</sup> and Haiyang Liao<sup>1</sup>

## Effects of Cable Sheath on Deformation Coordination between the Sensing Fiber and Sand

### Reference

Q. Luo, D. Zhang, H. Yimit, J. Su, H. Wang, and H. Liao, "Effects of Cable Sheath on Deformation Coordination between the Sensing Fiber and Sand," *Geotechnical Testing Journal*  
<https://doi.org/10.1520/GTJ20230370>

### ABSTRACT

Distributed fiber optic sensing has been used for monitoring land subsidence, and accurate measurement of soil deformation relies on the coordination between the optical fiber and soil, also known as the deformation coordination between the optical fiber and soil ( $DC_{f-s}$ ). To investigate this issue, three types of optical cables with different sheath structures were embedded in triaxial specimens made of standard sand. The fiber strain was measured by optical frequency domain reflectometry. The axial deformation of the specimen was measured by a linear variable displacement transducer sensor. Each specimen was subjected to 12 loading and unloading cycles under varying axial stresses, confining pressures, and dry or wet conditions during the triaxial tests. Results shows that the  $\Phi 3$  mm loose-tube optical cable has poor  $DC_{f-s}$  with the strain not exceeding  $15 \mu\epsilon$ . Under a confining pressure of 200 kPa, 400 kPa, and 500 kPa, the  $DC_{f-s}$  coefficients between the  $\Phi 3$  mm tight-buffered optical cable and wet sand during loading are 0.266, 0.366, and 0.496, respectively. The  $DC_{f-s}$  coefficients of the  $\Phi 5$  mm tight-buffered optical cable under identical conditions are 0.186, 0.226, and 0.249. Overall, the  $\Phi 3$  mm tight-buffered optical cable exhibits superior  $DC_{f-s}$  compared with both the  $\Phi 5$  mm tight-buffered optical cable and  $\Phi 3$  mm loose-tube optical cable, indicating that the sheath structure is a crucial factor in determining the  $DC_{f-s}$ . In addition, the  $DC_{f-s}$  is also influenced by several other factors, including the number of loading-unloading cycles and the confining pressure in the soil.

### Keywords

distributed fiber optic sensing, deformation coordination, optical fiber, triaxial test, land subsidence

Manuscript received April 4, 2023; accepted for publication February 29, 2024; published online July 2, 2024.

<sup>1</sup> School of Earth Sciences and Engineering, Nanjing University, No. 163 Xianlin Ave., Qixia District, Nanjing, Jiangsu Province 210023, China, <https://orcid.org/0009-0003-3752-0237>

<sup>2</sup> School of Earth Sciences and Engineering, Nanjing University, No. 163 Xianlin Ave., Qixia District, Nanjing, Jiangsu Province 210023, China (Corresponding author), e-mail: [zhangdan@nju.edu.cn](mailto:zhangdan@nju.edu.cn)

<sup>3</sup> China Geological Survey, Nanjing Center, No. 534, Zhongshan E. Rd., Qinhua District, Nanjing 210016, China

## Introduction

Deformation on the earth's surface can be caused by human activity, tectonic processes, or a combination of these factors. Widespread surface deformation (e.g., subsidence, uplift) can occur when a large volume of fluid is withdrawn from or reintroduced to an underground reservoir system (Amer et al. 2021). Because of the population's rapid increase and industrial demand, a significant amount of groundwater is being used. The extraction of groundwater can generate land subsidence by causing the compaction of susceptible aquifer systems that comprise aquifers and aquitards (Wu et al. 2015).

Land subsidence is the gentle settling or rapid sinking of the ground surface due to the consolidation of sediments and thus the subsurface movement of earth materials as a result of increasing effective stress (Bagheri-Gavkosh et al. 2021). As a human- and naturally-induced geohazard (Liu, Ma, and Du 2017), land subsidence leads to much destruction of civil structures and causes loss and damage around the world (Calderhead et al. 2011). In China, intensive irrigation activities have been mapped over the North China Plain aquifer by global irrigation mapping studies, and land subsidence is already occurring on a large scale in other regions of the globe, such as Spain, Italy, the United Kingdom, and California and Texas (Hasan et al. 2023).

Deformation measurements at the early stages are crucial for evaluating and controlling land subsidence. Light detection and ranging (LiDAR)- and interferometric synthetic aperture radar (InSAR)-based technologies have become the main string in monitoring land deformation (Fan et al. 2011; Dehghani et al. 2013; He et al. 2021). However, these methods cannot measure the underground deformation at different depths. In recent years, distributed fiber optic sensing (DFOS) has been used to obtain profiles and detailed distributions of subsurface deformation (Wu et al. 2021), to reveal the mechanisms of land subsidence (Gu et al. 2018) and to predict and evaluate land subsidence (Liang et al. 2022). DFOS can obtain the strain and temperature changes along an optical sensing fiber (Liu et al. 2020), which offers the possibility of truly distributed measurement (Barrias, Casas, and Villalba 2016). DFOS is a breakthrough monitoring method for geological disasters, such as landslides, land subsidence, and ground deformation (Zhang et al. 2020). The optical sensing fiber is similar to a sensory neural network embedded in a "dead" geological body, the changes of which can be monitored in one to three dimensions (Shi et al. 2021). Moreover, DFOS technology has the features of accurate and reliable measurements, possibility of assessing shape and displacements, detection of local damages, high durability, etc. (Kulpa et al. 2021).

When monitoring strain distribution in a material, strain transfer will be affected by bonding characteristics between the material and the optical fiber (Ansari and Libo 1998). Thus, the key to applying DFOS in geoenvironmental engineering is a well-grounded understanding of the deformation coordination between the optical fiber and geomaterials. Chen and Zhang (2011) first proposed a pullout test to examine the deformation coordination between the optical fiber and geomaterials. A simplified model describing the progressive failure of a fiber-soil interface was briefly illustrated (Zhang et al. 2015). However, the optical sensing cable is in an actively deformed status under the pullout load, which may lead to a significantly nonhomogeneous strain distribution and a reduced diameter of the optical cable. Wu et al. (2020) investigated the deformation coordination between the optical fiber and sand in a triaxial compression condition, which is more in-line with the field conditions of land subsidence because the optical sensing cable is passively deformed when the sand layer is compressed on account of the land subsidence. In other words, the deformation of the fiber is transferred from the compressed sand.

The sheath of the optical sensing cable is one of the main influences on the deformation coordination between the optical fiber and soil ( $DC_{f-s}$ ). In this study, a triaxial test was designed to investigate the  $DC_{f-s}$  for the optical sensing cables with different sheath structures. The axial strain distribution of the sand specimens was measured by three types of embedded optical cables. A strain transfer model was established by considering the strain attenuation between the optical fiber and sand. The results are the theoretical support in the analysis of strains monitored by different optical sensing cables.

## Materials and Methods

### SAND AND OPTICAL SENSING CABLES

A triaxial test was conducted to investigate deformation coordination between the optical fiber and soil. The China International Organization for Standardization standard sand (CISS), with particle sizes ranging from 0.08–2.0 mm, was chosen for the triaxial specimens because it is widely used as a common material in borehole backfilling. The physical and mechanical properties of CISS are given in [Table 1](#). The grain size distribution curve of CISS is shown in [figure 1](#).

Optical sensing cables for ground deformation monitoring often incorporate multilayer buffers and sheaths to increase their robustness. Optical cables with steel strand-forced have been employed for field monitoring of strain distribution ([Gao et al. 2006](#)). In addition, some applications of  $\Phi 3$  mm tight-buffered optical cables in strain measurement were reported ([Sun et al. 2014](#); [Sasaki et al. 2021](#)). In fact, a wide variety of structural types of sensing cables have been used for fiber optic monitoring ([Sang et al. 2019](#)).

Thus, three types of optical cables with different sheath structures, including  $\Phi 3$  mm tight-buffered optical cables (TOC),  $\Phi 5$  mm tight-buffered optical cables, and  $\Phi 3$  mm loose-tube optical cables (LOC) were adopted for the tests. The  $\Phi 3$  mm loose-jacketed fiber optic cables were selected for comparison. The physical and mechanical properties of the optical cables are shown in [Table 2](#), and detailed structures of these three types of optical cables are elaborated in the section titled “Strain Transfer Model.”

### TRIAXIAL APPARATUS

A triaxial testing apparatus in which an optical sensing cable can be implanted was designed to investigate the  $DC_{f-s}$ , as shown in [figure 2](#). The size of the plexiglass pressure chamber is 620 mm high and 306 mm in diameter. The pressure chamber is filled with water and is used to apply confining pressure to the sand specimen. The deviator stress is applied by a controllable servo motor.

**TABLE 1**

Basic physical properties of CISS

Specific Gravity, $G_s$	Diameter, mm	Internal Friction Angle $\varphi$ , °	Coefficient Uniformity $C_u$	Coefficient of Curvature $C_c$	Water Content of Wet Sand, %
2.67	0.08–2.0	25.64	3.04	0.71	11.24

**FIG. 1**

The grain size distribution curve of CISS.

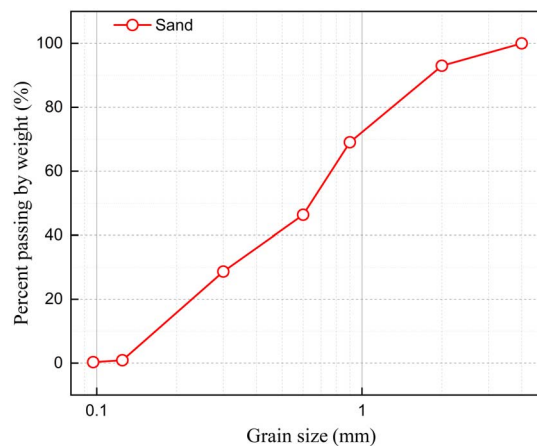
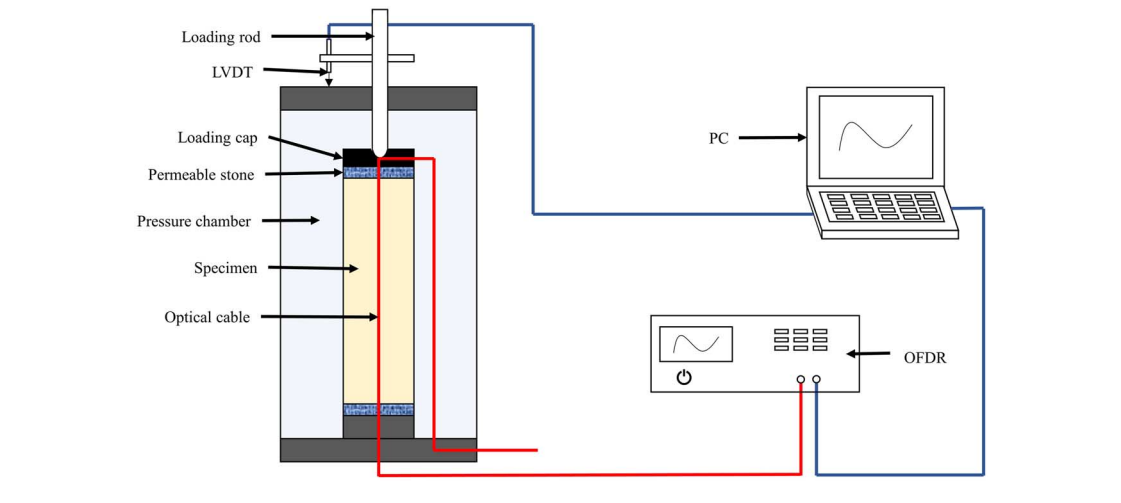


**TABLE 2**  
Basic physical and mechanical parameters of optical sensing cables

	$\Phi 3$ mm TOC	$\Phi 5$ mm TOC	$\Phi 3$ mm LOC
Coating Material	Acrylate		
Sheath material	Low temperature resistant Polyurethane (PU) and Hytrel	Low temperature resistant Polyurethane (PU), Hytrel, and Steel strand	Polyvinyl chloride (PVC) and Kevlar fiber
Fiber count	1		
Fiber category	Single mode (G652B)		
Curvature radius, mm	18	30–50	18
Radius of core and cladding $r_f$ , mm	0.063		
Elastic modulus of core and cladding $E_f$ , GPa	72		
Radius of coating $r_c$ , mm	0.125		
Shear modulus of coating $G_c$ , MPa	1		
Radius of sheath $r_j$ , mm	1.39	2.375	1.39
Nominal shear modulus of sheath $G_j$ , MPa	50	75	2.7
Radius of outer jacket $r_o$ , mm	3	5	3
Shear modulus of outer jacket $G_o$ , MPa	20	18	10

**FIG. 2** Schematic diagram of the triaxial testing apparatus.



The axial deformation of the specimen was measured by a linear variable displacement transducer (LVDT) sensor. The axial strain distribution inside the specimen was monitored by the optical sensing cable passing through the chamber and connecting to optical frequency domain reflectometry (OFDR).

OFDR is a strain sensor with high spatial resolution and sensing accuracy that localizes the scattered signal by measuring the frequency of the Rayleigh scattered signal generated by the modulated detector light (Wang et al. 2023). It is used to collect the axial strain distribution of the specimen during the test. Specific parameters of OFDR are shown in Table 3.

### TEST CONDITIONS AND PROCEDURE

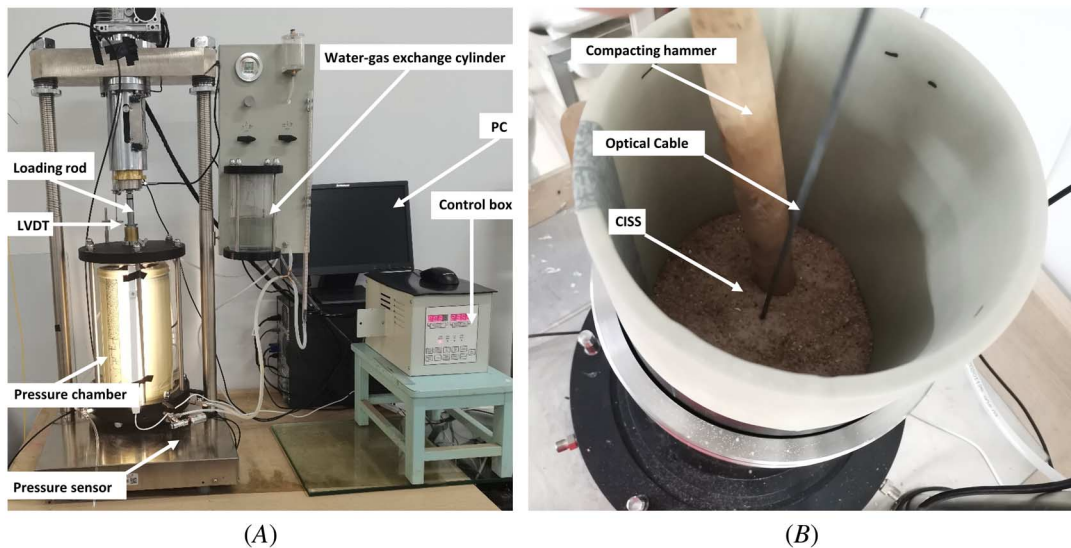
Three stages are included in the triaxial test.

- (1) Specimen preparation: The dry sand was filled in a sample mold with an optical cable embedded in the specimen, as shown in figure 3B. The sand was tamped layer by layer. The dry density is  $0.17 \text{ g/cm}^3$ .

**TABLE 3**  
Specific parameters of OFDR

Parameter	Parameter Indicators
Spatial resolution, mm	1/2/5/10
Sensing distance, m	20/50/100
Strain measurement accuracy, $\mu\epsilon$	$\pm 1$
Strain measurement range, $\mu\epsilon$	$\pm 12,000$
Temperature measurement accuracy, $^{\circ}\text{C}$	$\pm 0.1$
Temperature measurement range, $^{\circ}\text{C}$	$-200$ 1,200

**FIG. 3** Triaxial test: (A) test apparatus and (B) specimen preparation.

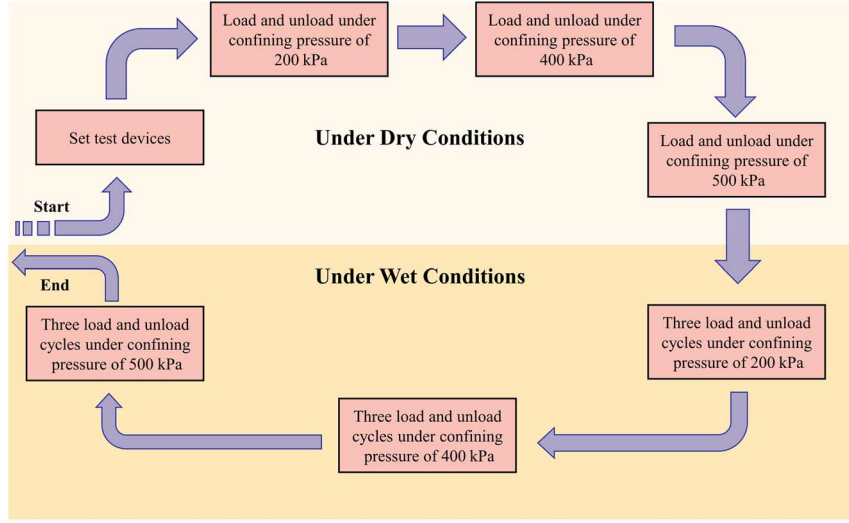


The specimen size was  $300 \pm 5$  mm high and 150 mm in diameter. The optical cable was kept straight during sand filling and tamping.

- (2) Mold removal: After completion of specimen construction, a negative pressure should be applied immediately on the specimen to avoid collapsing after removing the mold. In this test, the negative pressure was kept within the range of  $-15$  to  $-25$  kPa.
- (3) Cyclic loading–unloading tests: The dry specimens were tested in one loading–unloading cycle. Afterward, the specimen was wet. The water content of wet specimens was 11.24 % and kept constant during the following tests. Three loading–unloading cycles on the same wet specimen were conducted. A detailed test scheme is given in [Table 4](#). In total, 12 loading–unloading cycles were performed for each specimen under different confining pressures, including 3 cycles under dry conditions and 9 cycles under wet conditions. The test flow is shown in [figure 4](#).

**TABLE 4**  
Test scheme

Confining Pressure, kPa	Deviator Stress, kPa
200	0, 25, 50, 75, 100, 75, 50, 25, 0,
400	0, 50, 100, 150, 200, 150, 100, 50, 0
500	0, 50, 100, 150, 200, 250, 200, 150, 100, 50, 0

**FIG. 4** Flow chart of the tests.


## Strain Transfer Model

A borehole is typically drilled to conduct a comprehensive investigation of the strata deformation resulting from land subsidence. The optical sensing cables are installed in the borehole with backfill material full-filled, as shown in [figure 5A](#). When land subsidence occurs, the soil undergoes deformation due to changes in vertical and horizontal stress, which can lead to the deformation of the embedded optical cables as illustrated in [figure 5B](#).

The detailed structure of the optical sensing fiber is shown in [figure 6](#). The fiber is encased in a protective layer, including the sheath and coating. As a result, a portion of the strain is absorbed by the protective layer when the soil strain is transferred to the fiber, which leads to a disparity in strain between the optical fiber and soil. A strain transfer model is established to discuss the characteristics of strain transformation between the optical fiber and soil.

A three-layers strain transfer model consisting of “soil-protective layer-fiber” was developed, as depicted in [figure 7](#). To simplify the analysis, the following assumptions are made ([Ansari and Libo 1998](#); [Li et al. 2006](#)).

- (1) The core and cladding layers of the fiber are both composed of silica, and together they are considered the fiber layer in the strain transfer model.
- (2) The coating, sheath, and out jacket of optical cables are considered protective layers. The overall shear modulus of the protective layer is calculated by weighing the volume of each part.
- (3) The soil and fiber material under test are in-line with the principles of linear elasticity.
- (4) The interfaces of the fiber, protective layer, and soil are tightly bonded with no slippage.
- (5) The interface between the protective layer and soil has only shear stress.
- (6) The optical cable has no impact on the overall strain distribution of the soil, and the strain distribution of the soil is uniform.

The parameters in the strain transfer model are illustrated in [figures 7 and 8](#), in which  $\sigma$  represents the axial normal stress,  $u$  denotes the axial deformation, and  $\tau$  signifies the interfacial shear stress.

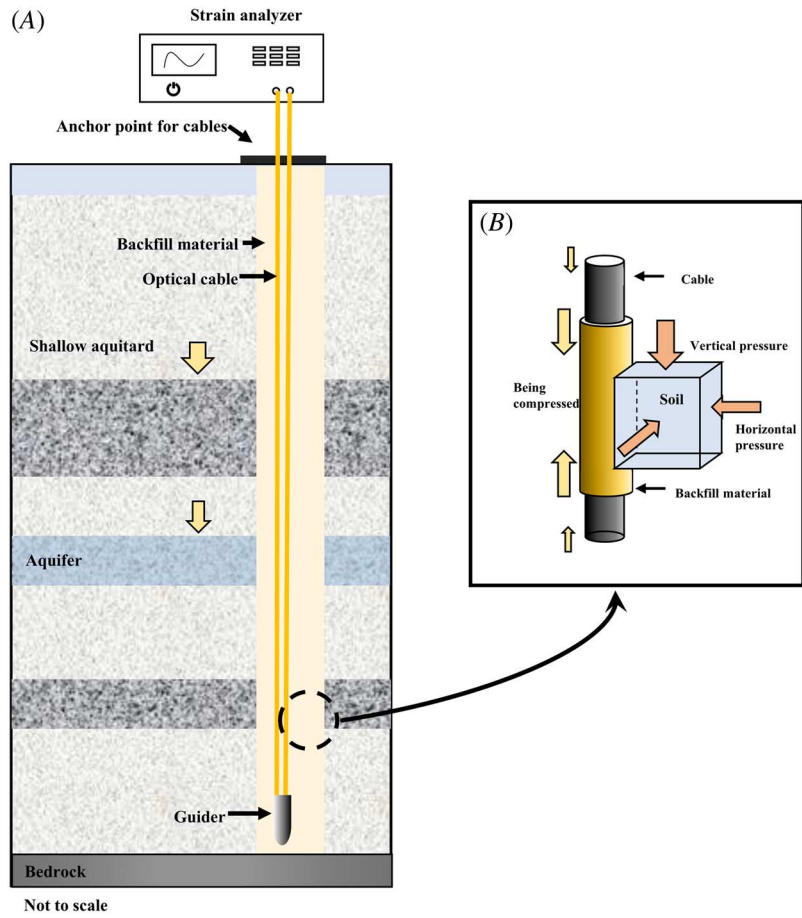
The hydrostatic equilibrium conditions of the fiber and protective layer are as follows:

$$\pi r_f^2 d\sigma_f = \tau_{pf} 2\pi r_f dz \quad (1)$$

$$(\pi r_p^2 - \pi r_f^2) d\sigma_p + \tau_{pf} 2\pi r_f dz - \tau_{sp} 2\pi r_p dz = 0 \quad (2)$$

**FIG. 5**

Monitoring scheme for land subsidence using DFOS: (A) sensing cable installation in a borehole and (B) pressures in the soil and deformation of the backfill material and cable.



The geometric equations are as follows:

$$u_s(r, z) = \int_0^z \epsilon_s dz \quad (3)$$

$$u_f(r, z) = \int_0^z \epsilon_f dz \quad (4)$$

$$\delta_p = \int_{r_f}^{r_p} \frac{\tau(r, z)}{G_p} dr \quad (5)$$

where:

$\epsilon_s$  = the axial strain of the soil,

$\epsilon_f$  = the axial strain of the fiber,

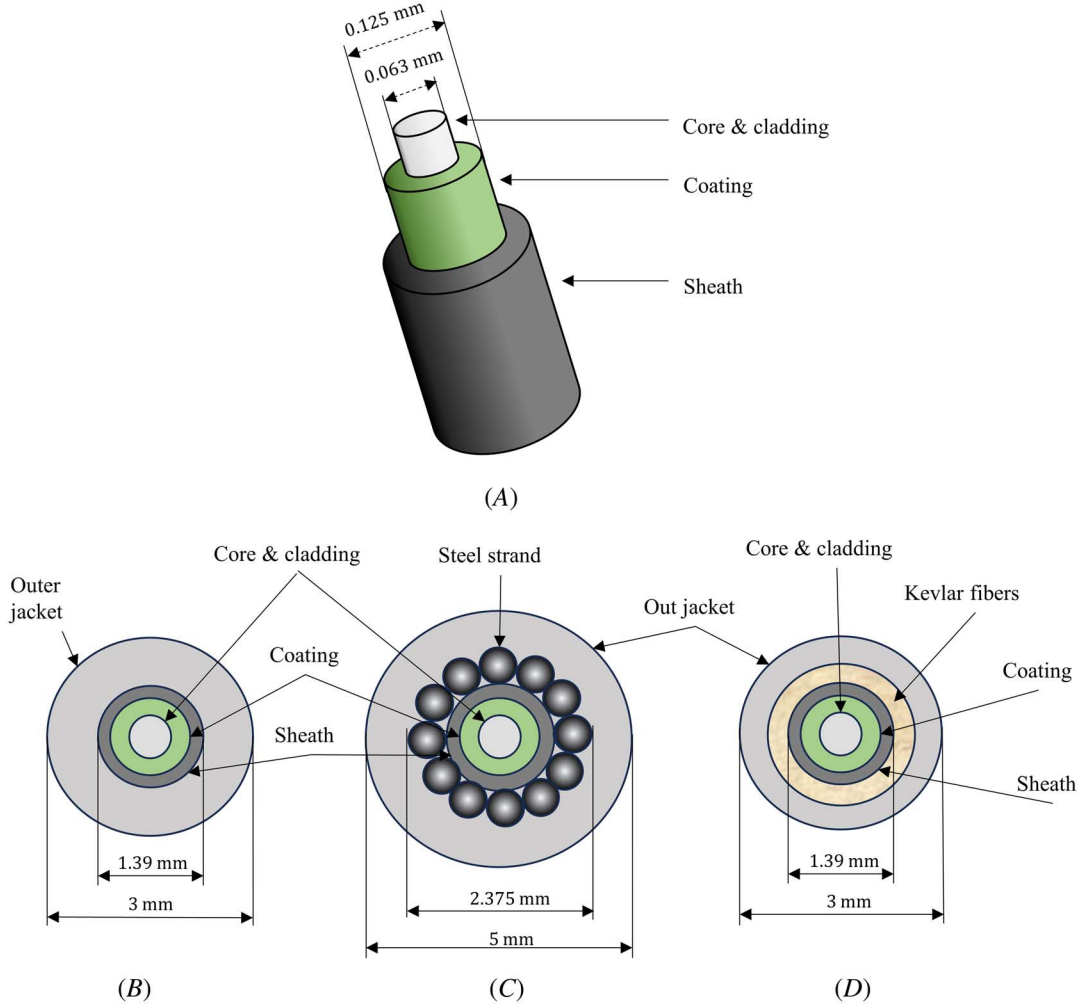
$\delta_p$  = the relative displacement difference between the fiber and soil, and

$G_p$  = the shear modulus of the protective layer.

$$u_p(r_p, z) - u_p(r_f, z) = \delta_p \quad (6)$$



**FIG. 6** Structure of an optical sensing cable: (A) the basic structure of an optical cable; structure of (B)  $\Phi 3$  mm TOC, (C)  $\Phi 5$  mm TOC, and (D)  $\Phi 3$  mm LOC.



The deformation coordination equation is as follows:

$$\frac{\tau(r, z)}{\tau_{sp}(r_p, z)} = \frac{r_p}{r} (r_f \leq r \leq r_p) \quad (7)$$

It is assumed that there is no slippage at the interface between the protective layer and the soil, as well as the interface between the protective layer and the fiber; therefore, the following:

$$u_p(r_f, z) = u_f(r_f, z) \quad (8)$$

$$u_s(r_p, z) = u_p(r_p, z) \quad (9)$$

**FIG. 7** Stress analysis on an element.  $r$ ,  $\tau$ , and  $\sigma$  represent radius, shear stress, and normal stress. Subscripts,  $s$ ,  $p$ , and  $f$  denote the soil, protective layer, and fiber. Combined subscripts,  $sp$ , and  $pf$ , denote the interface between soil and protective layer, and the interface between fiber and protective layer.

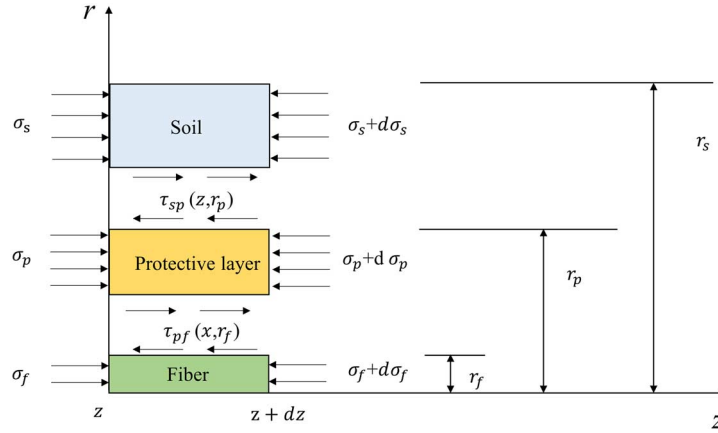
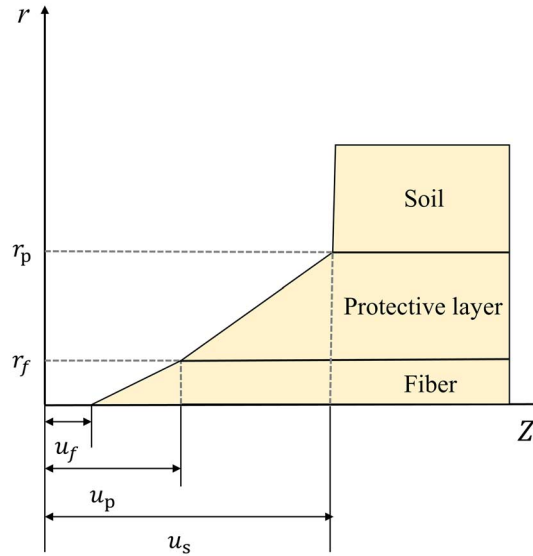


**FIG. 8**

Deformation relationship of the strain transfer model.  $r$  and  $u$  represent radius and deformation. Subscripts,  $s$ ,  $p$ , and  $f$ , denote soil, protective layer, and fiber.



Assume that the strain distribution of soil is  $\varepsilon_s(z)$ , and from equations (6), (8) and (9), we have the following:

$$u_s(r_p, z) - u_f(r_f, z) = \delta_p \quad (10)$$

After substituting equations (3)–(5) and equation (7) into equation (10), the second-order derivative of both sides of the equation with respect to  $z$  is taken, which yields the following:

$$\frac{d\varepsilon_s(z)}{dz} - \frac{1}{E_f} \frac{d\sigma_f(r_f, z)}{dz} = \frac{r_p}{G_p} \ln \frac{r_p}{r_f} \frac{d^2 \tau_{sp}(z)}{dz^2} \quad (11)$$

By equation (7), when  $r = r_f$ , then the following:

$$\tau_{pf}(z) = \frac{r_p}{r_f} \tau_{sp}(z) \quad (12)$$

Substituting equation (11) and equation (12) into the hydrostatic equilibrium conditions, we obtain the following:

$$\frac{d^2 \tau_{sp}(z)}{dz^2} - c^2 \tau_{sp}(z) = k \frac{d\varepsilon_s(z)}{dz} \quad (13)$$

where

$$c = \sqrt{\frac{2G_p}{r_f^2 E_f \ln \frac{r_p}{r_f}}}, \quad k = \frac{G_p}{r_p \ln \frac{r_p}{r_f}} \quad (14)$$

When the axial strain distribution of the specimen is uniform, equation (13) becomes the following:

$$\frac{d^2 \tau_{sp}(z)}{dz^2} - c^2 \tau_{sp}(z) = 0 \quad (15)$$

The boundary conditions are as follows:

$$\varepsilon_f(-L) = \varepsilon_f(L) = 0 \quad (16)$$

$$\tau_{sp}(0) = 0 \quad (17)$$

Therefore, the solution is as follows:

$$\tau_{sp}(z) = \frac{c E_f r_f^2}{2 r_p (\cosh(cL) - 1)} \varepsilon_s \sinh(cz) \quad (18)$$

From equation (12) and the hydrostatic equilibrium conditions, we have as follows:

$$\varepsilon_f(z) = \frac{2 r_p}{E_f r_f^2} \int_{-L}^z \tau_{sp}(0) dz \quad (19)$$

Combining equation (18) and equation (19), we obtain the following:

$$\varepsilon_f(z) = \varepsilon_s \left( 1 - \frac{\cosh(cz) - 1}{\cosh(cL) - 1} \right) \quad (20)$$

By defining the ratio of fiber strain to soil strain  $\alpha(z)$  as the strain transfer rate, we have the following:

$$\alpha(z) = \frac{\varepsilon_f(z)}{\varepsilon_s(z)} = 1 - \frac{\cosh(cz) - 1}{\cosh(cL) - 1} \quad (21)$$

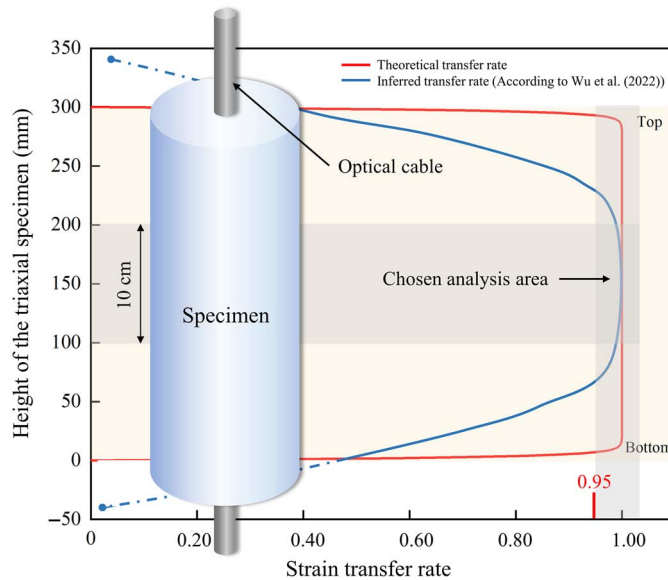
The average strain transfer rate refers to the relationship between the average strain experienced by both the fiber and the surrounding soil along the length of the fiber. Specifically, it is calculated as the ratio of the average strain of the fiber to the average strain of the soil over the length of the fiber.

$$\alpha = \frac{\int_0^L \varepsilon_f(z) dz}{\varepsilon_s(z) L} = 1 - \frac{\sinh(cL) + cL}{cL(\cosh(cL) - 1)} \quad (22)$$

The strain distribution of the optical fiber inside the specimen can be calculated theoretically using the parameters in [Tables 2](#) and [3](#) based on the assumption of uniform strain.

**FIG. 9**

Distribution of theoretical strain transfer rate and actual strain along the height of specimen.



The distribution for the theoretical strain transfer rate  $\alpha$  of the optical fiber buried in the soil is shown in **figure 9**.  $\alpha$  is larger than 0.95 from the specimen height of 8 mm to 292 mm, which is considered a high-strain sensing section. The measured strain in the high-strain sensing section is supposed to be accurate theoretically. At both ends of the specimen, there is a low-strain sensing section in which the value of  $\alpha$  is less than 0.95 because of the sheath effect caused by the optical cable's protective layer. For actual monitoring, the sheath effect will result in a smaller strain at both ends of the specimen and produce epitaxial strain along the optical fiber outside the sample, as well (Wu et al. 2022). Obviously, the strain in the low-strain sensing section is dramatically influenced by the sheath effect. Therefore, the strain distribution of the optical sensing cable that is within 10 cm of the specimen's middle is chosen for analysis of the deformation coordination between the optical fiber cable and soil.

The red line represents the theoretical transfer rate at the height of the specimen calculated using equation (22). The blue line represents a schematic diagram of the actual transfer rate drawn based on the research results of Wu et al. (2022).

## Results and Discussion

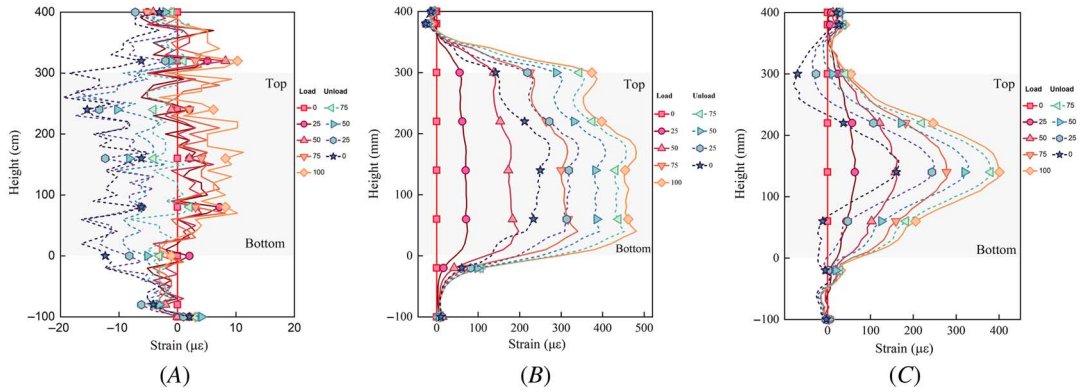
### STRAIN DISTRIBUTION UNDER DRY CONDITIONS

#### Effects of Sheath Structure

Three different optical cables with varied sheath structures were tested, and the measured strain distribution throughout the specimens showed substantial variations. **Figure 10** depicts the axial strain distributions measured by the cables.

The measured strain distribution of  $\Phi 3$  mm LOC is significantly different from the theoretical distributions, and the strain value is less than  $15 \mu\epsilon$  during the loading–unloading cycle, as shown in **figure 10A**. Obviously, the LOC cannot be used to monitor the soil deformation because the diameter of the optical fiber is smaller than the inner diameter of the tube and the fiber can move freely in the tube. The mechanical loads on the optic cable are mainly undertaken by the sheath. Therefore, the strains along the fiber core were small and irregular during the triaxial tests because the deformation of the sand is buffered by the loose-tube structure of the LOC.

**FIG. 10** Strain distribution of (A)  $\Phi 3$  mm LOC, (B)  $\Phi 3$  mm TOC, and (C)  $\Phi 5$  mm TOC in the dry specimens under a confining pressure of 200 kPa.



Theoretically, the distribution of strains inside the specimen is uniform during the elastic deformation of the specimen, which means that the strains at both ends of the specimen shall be equal to the strains in the middle. The strain of  $\Phi 3$  mm TOC shows a D-shaped distribution and the strain is basically uniformly distributed in the middle of the specimen as shown in [figure 10B](#), which is consistent with the theoretical analysis. However, the strain of the optical fiber does not drop abruptly to zero at either end of the specimen because of the sheath effect. Meanwhile, a decreasing strain can also be found outside the specimen because of the sheath effect.

The sheath of  $\Phi 5$  mm TOC is thicker and the modulus of  $\Phi 5$  mm TOC is higher than that of the  $\Phi 3$  mm TOC because the sheath of  $\Phi 5$  mm TOC is strengthened by steel strands, which have a stronger impact on strain transfer from the soil to the optical fiber. Therefore, the measured strain by  $\Phi 5$  mm TOC decreases from the middle to both ends of the specimen, as shown in [figure 10C](#). The fiber strain of  $\Phi 5$  mm TOC shows a smooth single-peak distribution during the loading–unloading cycle, which indicates that the sheath effect of  $\Phi 5$  mm TOC is more significant. In addition, the  $\Phi 5$  mm TOC has a longer epitaxial length, and the strain at both ends of the specimen is larger, which also means that the sheath effect is obvious.

The sensing performance of the two types of TOC is investigated by the measured strain in the middle of the specimen. The strain of TOCs under dry conditions and at the confining pressure of 200 kPa are shown in [Table 5](#). The strain of  $\Phi 3$  mm TOC is larger than that of  $\Phi 5$  mm TOC, which indicates that  $\Phi 3$  mm TOC has a better performance on the strain transfer as  $\Phi 3$  mm TOC has thinner and simpler sheath with smaller

**TABLE 5**  
Maximum strains of two types of TOC in the middle of dry specimens

Process	Deviator Stress, kPa	Strains of $\Phi 3$ mm TOC, $\mu\epsilon$	Strains of $\Phi 5$ mm TOC, $\mu\epsilon$
Loading	0	0	0
	25	69.9	63.7
	50	178.9	158.3
	75	315.7	227.6
	100	481.2	401.1
Unloading	75	456.5	380.4
	50	407.2	319.8
	25	341.3	243.7
	0	271.4	160.4

sheath modulus. To summarize, the sheath structures of the optical sensing cable have a significant impact on the fiber strain.

### EFFECTS OF SAND PLASTICITY

A layered tamping method was adopted during the specimen preparation, which may result in uneven density within the sample. Therefore, the measured strain may not be uniform, as illustrated by the uneven strain of  $\Phi 3$  mm TOC in the middle of the specimen, as shown in [figure 10B](#).

[Table 6](#) shows the measured strain in the middle of the specimen by using  $\Phi 3$  mm TOC during a loading–unloading cycle. The fiber strain in the unloading process is always greater than that in the loading process under the same deviator stress, which means that the plastic deformation of soil occurs during the tests and can be monitored by the optical fiber. The plastic strain can be verified by LVDT under a confining pressure of 200 kPa, as shown in [Table 7](#), which is calculated by the following formula.

$$E_{LVDT} = \frac{D_U - D_L}{300} \cdot 10^6 \quad (23)$$

where  $\varepsilon_{LVDT}$  is the plastic strain measured by LVDT,  $D_U$  is the deformation during unloading, and  $D_L$  is the deformation during loading.

By comparing [Tables 6](#) and [7](#), the plastic strains measured by the  $\Phi 3$  mm TOC are close to, but generally lower than, those measured by LVDT. In addition, the deformation of the specimen during unloading is typically larger than that during loading under the same deviator stress. As a result, the strain characteristics of the optical sensing fiber are somewhat different between loading and unloading because of the sand plasticity. The fiber strain may be influenced by the soil plasticity.

### STRAIN DISTRIBUTION UNDER WET CONDITIONS

[Figure 11](#) shows the stress–strain curves of a wet specimen in three loading–unloading cycles according to the measurement of LVDT. The hysteresis loop further proves the plastic deformation of the sand.

The first cycle exhibits the most prominent hysteresis phenomenon. However, the hysteresis effect weakens as the loose soil undergoes loading–unloading cycles and gradually compacts. It can be inferred that the contact

**TABLE 6**

Maximum strain of the  $\Phi 3$  mm TOC under a confining pressure of 200 kPa for dry specimen

Deviator Stress, kPa	Strain during Loading, $\mu\epsilon$	Strain during Unloading, $\mu\epsilon$	Plastic Strain, $\mu\epsilon$
0	0	269.4	269.4
25	69.9	338.3	268.4
50	178.9	404.1	225.2
75	312.6	455.5	142.9
100	479.2	...	...

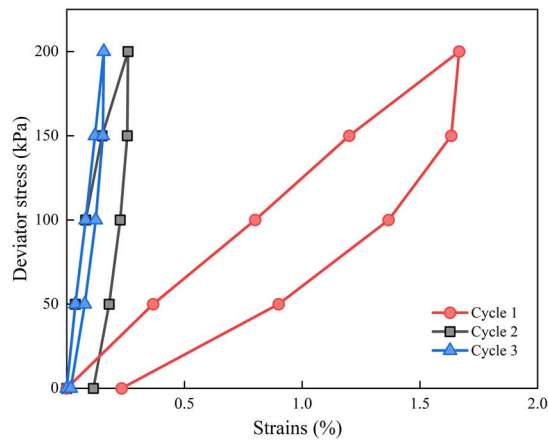
**TABLE 7**

Deformation measured by LVDT under a confining pressure of 200 kPa for dry specimen

Deviator Stress, kPa	Deformation during Loading, mm	Deformation during Unloading, mm	Plastic Strain, $\mu\epsilon$
0	0	0.07	233.3
25	0.09	0.21	400.0
50	0.27	0.37	333.3
75	0.36	0.44	266.7
100	0.45	...	...

**FIG. 11**

Stress–strain curve of wet specimen under a confining pressure of 400 kPa.



between the soil particles and the optic sensing cable becomes increasingly stronger, and  $DC_{f-s}$  is significantly improved with loading–unloading cycles. Consequently, the third cycle is chosen for the analysis of the deformation coordination between the optical fiber and soil under wet conditions.

**Figure 12** shows the strain distributions obtained by  $\Phi 3$  mm TOC and  $\Phi 5$  mm TOC under wet conditions. The strain distributions in the middle of specimens were selected for the analysis to avoid the influence of the sheath effect.

**Figure 12A** illustrates the strain distribution under the confining pressure of 200 kPa. The strain values of  $\Phi 3$  mm TOC in the middle of specimen are 0  $\mu\epsilon$ , 51  $\mu\epsilon$ , 122  $\mu\epsilon$ , 206  $\mu\epsilon$ , 329  $\mu\epsilon$ , 296  $\mu\epsilon$ , 242  $\mu\epsilon$ , 177  $\mu\epsilon$ , and 144  $\mu\epsilon$  for different deviator stresses during loading and unloading. In comparison, the  $\Phi 5$  mm TOC exhibit lower strain values for the same deviator stresses, which are 0  $\mu\epsilon$ , 23  $\mu\epsilon$ , 82  $\mu\epsilon$ , 134  $\mu\epsilon$ , 197  $\mu\epsilon$ , 185  $\mu\epsilon$ , 141  $\mu\epsilon$ , 69  $\mu\epsilon$ , and 4  $\mu\epsilon$ , as illustrated in **figure 12B**. The strain values of  $\Phi 3$  mm TOC are consistently higher than those of  $\Phi 5$  mm TOC at all levels of confining pressure, as evidenced by the comparisons of **figure 12C** with **figure 12D**, and **figure 12E** with **figure 12F**. In other words, the thinner and simpler sheath structure of  $\Phi 3$  mm TOC allows for more effective transfer of soil deformation to the optical fiber.

**Figure 12E** represents the strain distribution at a confining pressure of 500 kPa. The strain is basically uniformly distributed inside the specimen when the deviator stress was increased from 0 kPa to 200 kPa, which indicates that the specimen is compressed uniformly in the axial direction. However, a peak occurs in the strain distribution of  $\Phi 3$  mm TOC when the deviator stress was increased from 200 kPa to 250 kPa, which shows that the soil deformation increases obviously in the middle of the specimen. The strain peak exists throughout the unloading stage. The stress–strain curve under a confining pressure of 500 kPa is illustrated in **figure 13**. The slope of the stress–strain curve changes when the deviator stress increases from 200 kPa to 250 kPa. The nonlinearity of the stress–strain curve indicates shear damage occurring in the middle of the specimen, which is consistent with the findings of the optical sensing cable.

There are two main distinctions in the strain distributions under wet and dry conditions. First, in terms of curve morphology, the offset between the loading and unloading curves is comparatively smaller under wet conditions. Second, the strain distribution in the middle of the specimen obtained using the  $\Phi 5$  mm TOC is approximately uniform in wet conditions, as shown in **figure 12B**, **12D**, and **12F**. The distribution of the  $\Phi 5$  mm TOC under wet conditions falls between the D-shaped curve type measured with  $\Phi 3$  mm TOC and the single-peak type measured with  $\Phi 5$  mm TOC under dry conditions. Both of these distinctions are due to the high density of the specimens after repeated cycling, which results in small plastic deformation.

**FIG. 12** Strain distributions of TOCs under wet conditions: strain distributions of  $\Phi 3$  mm TOC under confining pressures of (A) 200 kPa, (C) 400 kPa, and (E) 500 kPa, and strain distributions of  $\Phi 5$  mm TOC under confining pressures of (B) 200 kPa, (D) 400 kPa, and (F) 500 kPa.

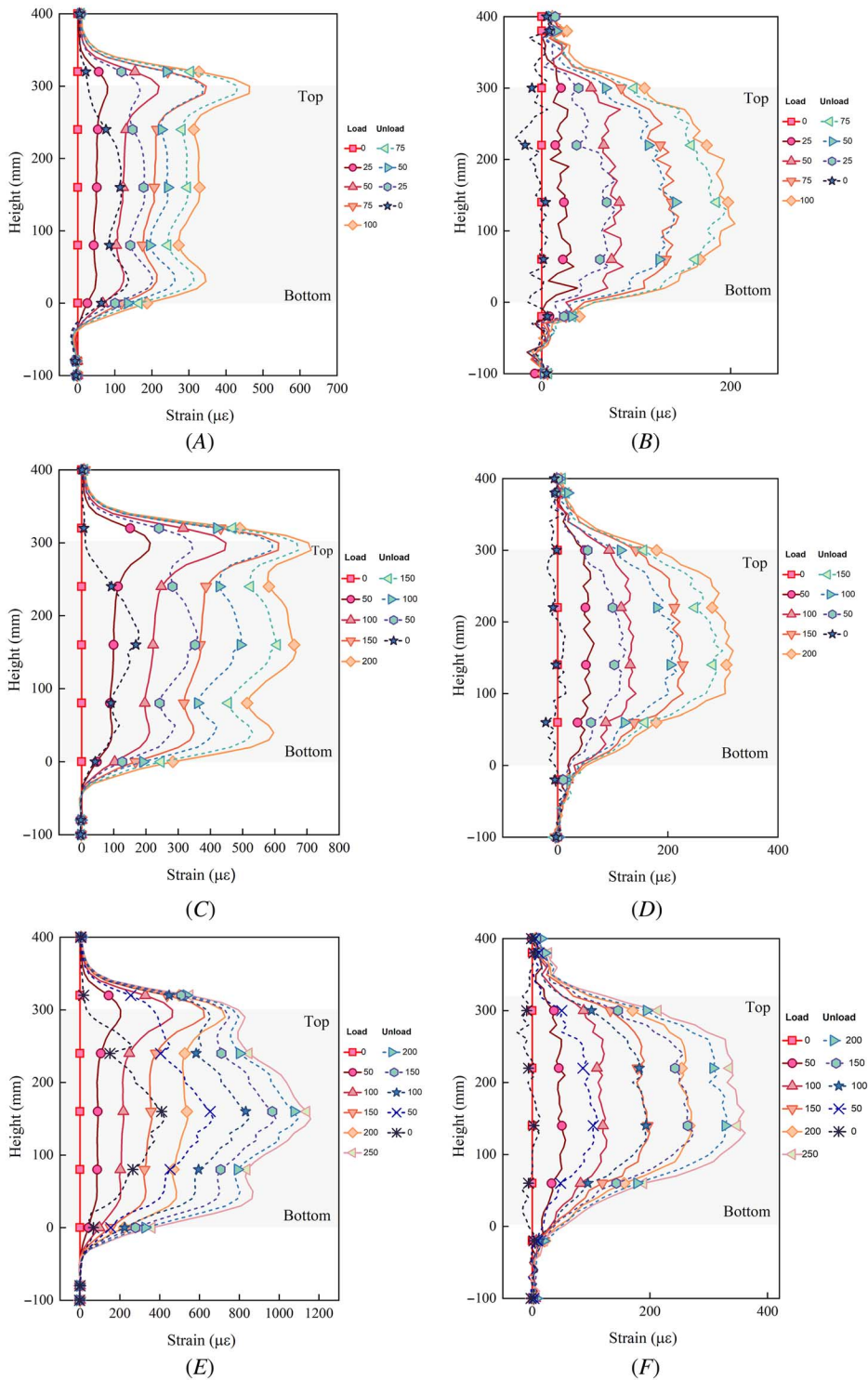
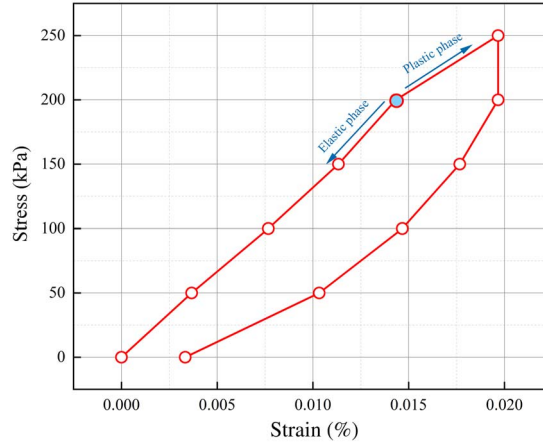




**FIG. 13**

Stress-strain curve of wet specimen in the third cycle under a confining pressure of 500 kPa.



The strains measured by optical cables are converted into deformation using equation (24).

$$d = \bar{\epsilon} \cdot 300 \quad (24)$$

where  $\bar{\epsilon}$  is the average strain within 10 cm of the middle of the specimen and  $d$  is the integral deformation measured by the optical fiber (mm).

The relative deviation of the measured deformation between DFOS and LVDT is calculated using equation (25).

$$\delta = \frac{d_{LVDT} - d_{OF}}{d_{LVDT}} \quad (25)$$

where  $\delta$  is the deviation between DFOS and LVDT,  $d_{LVDT}$  is the deformation obtained by LVDT, and  $d_{OF}$  is the deformation of optical fiber.

As shown in Table 8, the relative deviation for the  $\Phi 3$  mm TOC is higher compared with that of  $\Phi 5$  mm TOC, which indicates that the  $\Phi 3$  mm TOC has better deformation coordination, allowing for more efficient transfer of soil deformation to the optical fiber.

#### DEFORMATION COORDINATION BETWEEN THE OPTICAL FIBER AND SOIL ( $DC_{F-s}$ )

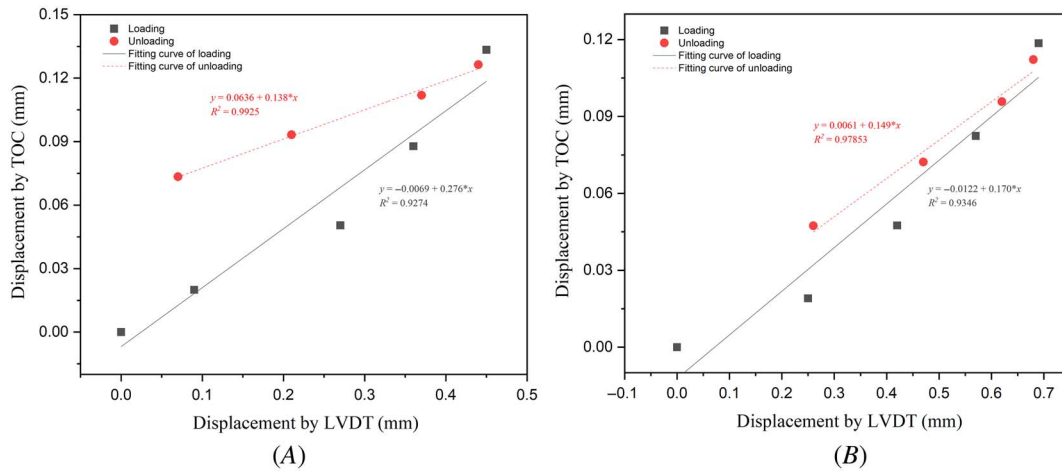
Based on the fiber-soil strain transfer model that relies on a uniform strain field, the deformation of the fiber is determined by integrating the fiber strain within 10 cm of the middle of the specimen according to equation (24).

**TABLE 8**

The deviation between DFOS and LVDT under wet conditions

Process	Deviator Stress, kPa	$\Phi 3$ mm TOC	$\Phi 5$ mm TOC
Loading	0	...	...
	25	89.88 %	82.30 %
	50	88.18 %	81.01 %
	75	87.15 %	82.78 %
	100	85.82 %	80.26 %
Unloading	75	87.80 %	81.49 %
	50	88.83 %	81.49 %
	25	89.41 %	84.10 %
	0	94.42 %	*NULL

**FIG. 14**  $DC_{f-s}$  for dry specimens under a confining pressure of 200 kPa, measured by (A)  $\Phi 3$  mm TOC and (B)  $\Phi 5$  mm TOC.



The  $DC_{f-s}$  can be determined by fitting the deformation of the fiber to the soil deformation measured by LVDT. The slope of the fitted line is defined as the  $DC_{f-s}$  coefficient.

#### DEFORMATION COORDINATION UNDER DRY CONDITIONS

Figure 14 shows the fitted line that represents the correlation between the deformation of the optical fiber and the soil deformation under dry conditions. The quality of the fitting is evaluated using the coefficient of determination  $R^2$ . A fitting result may be considered good if the  $R^2$  value is greater than 0.9. The  $R^2$  of fitting curves of  $\Phi 3$  mm TOC and  $\Phi 5$  mm TOC are both greater than 0.9, which indicates a good correlation between the deformation of the optical fiber and that of the specimen.

Theoretically, the  $DC_{f-s}$  coefficient of the fitting line is one if the deformations obtained by the optical fiber and LVDT are equal, which means that  $DC_{f-s}$  is perfect. In practice, the strains experience attenuation as they transfer from the soil to the optical fibers because of the protective layer of the cable. As a result, the  $DC_{f-s}$  coefficient is often less than one. Therefore,  $DC_{f-s}$  is thought to be better when the slope of the fitting line is closer to one. Even if  $DC_{f-s}$  coefficient is less than one, the deformation of the soil can still be determined based on the  $DC_{f-s}$  coefficient as long as there is a linear relationship between the deformation of the fiber optic and the soil deformation.

The  $DC_{f-s}$  coefficient of  $\Phi 3$  mm TOC during loading is 0.276 and that of  $\Phi 5$  mm TOC is 0.170, which is 64 % smaller than that of  $\Phi 3$  mm TOC. The  $DC_{f-s}$  of  $\Phi 3$  mm TOC is better than that of  $\Phi 5$  mm TOC because the sheath structure of  $\Phi 3$  mm TOC is thinner, simpler, and more tightly wrapped with the fiber.

The  $DC_{f-s}$  coefficient of the  $\Phi 3$  mm TOC during unloading is smaller than that during loading, as illustrated in figure 14A. A similar trend can also be observed for  $\Phi 5$  mm TOC. It can be inferred that the  $DC_{f-s}$  coefficient is related to the soil plasticity, as previously mentioned.

#### DEFORMATION COORDINATION UNDER WET CONDITIONS

The dry specimen is made wet by applying a hydrostatic pressure to obtain the  $DC_{f-s}$  under wet conditions. Figure 15 shows the fitting lines between the deformation of optical fiber and the soil deformation measured by LVDT under three different confining pressures, and the  $R^2$  value of all the curves is greater than 0.9.

The  $DC_{f-s}$  coefficients under wet conditions during loading range from 0.186 to 0.496 as shown in figure 15, which is generally higher than that under dry conditions ranging from 0.138 to 0.276 when the confining pressure

**FIG. 15**  $DC_{f-s}$  for wet specimens:  $DC_{f-s}$  between  $\Phi 3$  mm TOC and wet specimen under confining pressures of (A) 200 kPa, (C) 400 kPa, and (E) 500 kPa, and  $DC_{f-s}$  between  $\Phi 5$  mm TOC and wet specimen under confining pressures of (B) 200 kPa, (D) 400 kPa, and (F) 500 kPa.

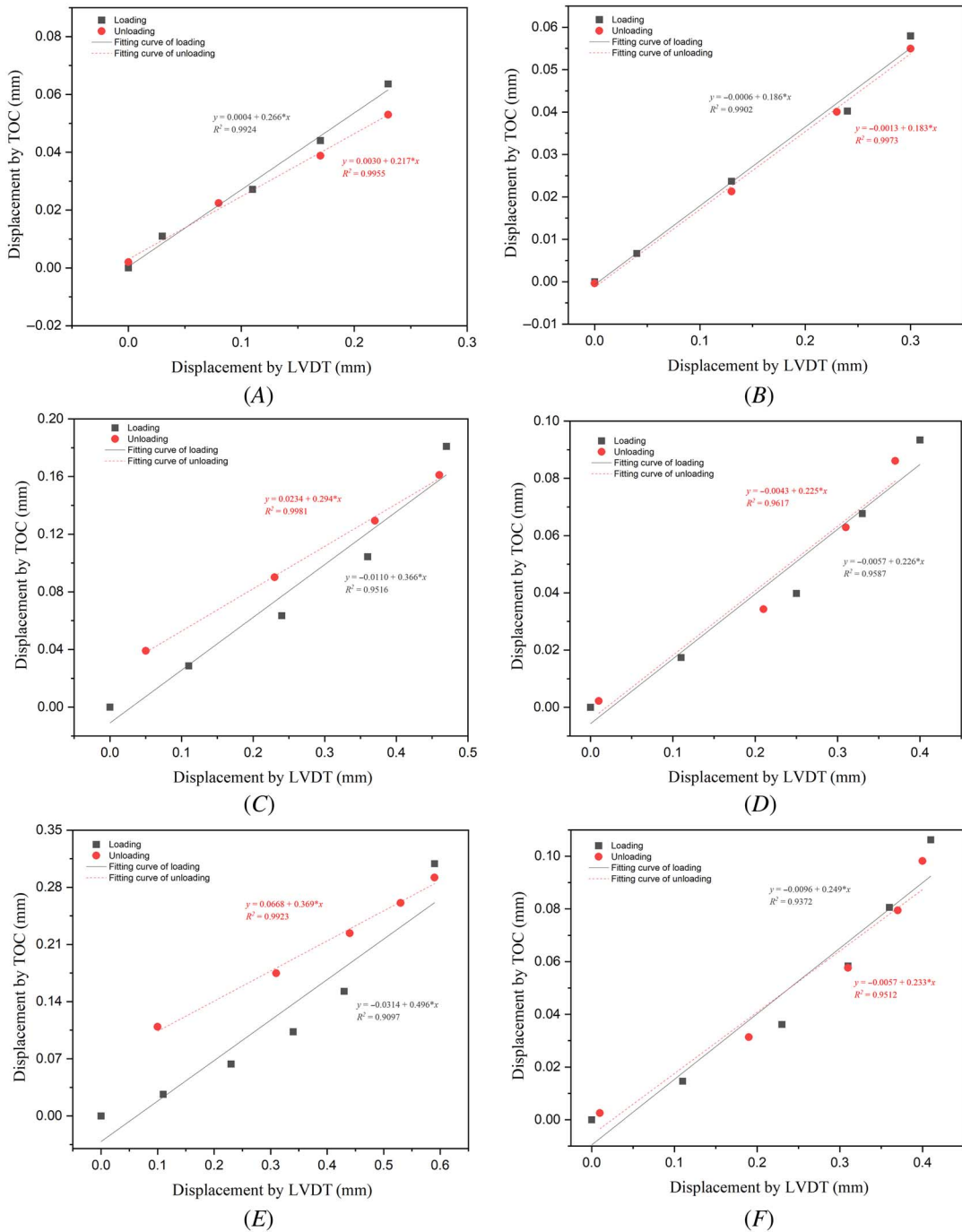
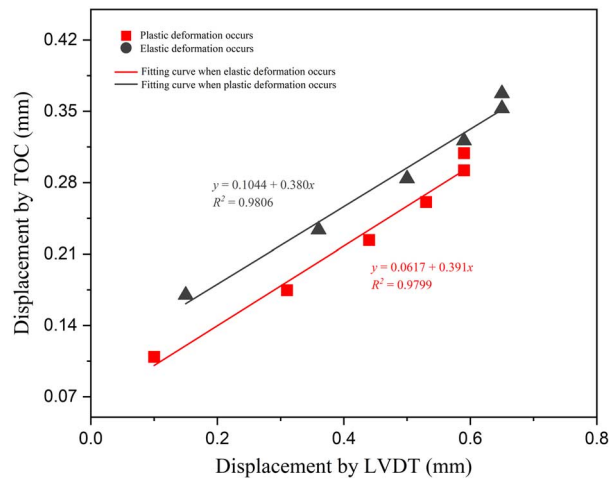


**FIG. 16**

Comparison of  $DC_{f-s}$  between elastic and plastic deformation.



and the type of optical cables are the same. This can be attributed to the additional loading–unloading cycles on the wet specimens, where water content of soil plays an utterly negative role in the optical cable–soil interfacial bond, making the  $DC_{f-s}$  worse.

Taking the loading process as an example, the  $DC_{f-s}$  coefficients of  $\Phi 3$  mm TOC are 0.266, 0.366, and 0.496 as the surrounding pressure increases from 200 kPa to 500 kPa (fig. 15A, 15C, and 15E) and that of  $\Phi 5$  mm TOC are 0.186, 0.226, and 0.249 (fig. 15B, 15D, and 15F). This trend is consistent for other conditions, as well. The  $DC_{f-s}$  of  $\Phi 3$  mm TOC is always better than that of  $\Phi 5$  mm TOC during loading and unloading under wet conditions because the  $DC_{f-s}$  coefficient of  $\Phi 3$  mm TOC is always higher than that of  $\Phi 5$  mm TOC. The results are consistent with the previous analysis, which indicated that the sheath structure of  $\Phi 3$  mm TOC has less influence on the deformation transfer between the fiber and soil. Therefore, the strain measured by  $\Phi 3$  mm TOC is more accurate than that measured by  $\Phi 5$  mm TOC.

There are three loading–unloading cycles under the same confining pressure. Therefore, the soil underwent several loading–unloading cycles and was gradually compacted when the confining pressure was increased from 200 kPa to 500 kPa. The increased sand density results in more contact points between the sand particles and the sheath, and the deformation transfer effect is enhanced. In addition, the friction between the sheath and sand particles is strengthened as the latter are embedded deeper into the cable sheath under high confining pressure. As a result of those mechanisms, the  $DC_{f-s}$  is improved.

While conducting the test with  $\Phi 3$  mm TOC, the specimen experienced shear damage under a confining pressure of 500 kPa and deviatoric stress loading ranging from 200 kPa to 250 kPa. The strain distribution is shown in figure 12E. The strain during unloading was selected for fitting to obtain the  $DC_{f-s}$  coefficient when the shear damage occurred in the specimen.  $DC_{f-s}$  coefficients under a confining pressure of 400 kPa are selected for the comparison with the coefficients obtained from the damaged specimen. The  $R^2$  values of both curves are greater than 0.95, as shown in figure 16. The  $DC_{f-s}$  coefficient of the plastic deformation is close to that of the elastic deformation, indicating that the plastic deformation of the soil has little effect on the  $DC_{f-s}$ .

Because of the sheath structure of the optical cable, the strain transfer between the optical cable and soil is weakened, resulting in a lack of coordination in their deformation. As a result, the deformation of the optical cable is smaller than that of soil, leading to a  $DC_{f-s}$  coefficient of less than one. Nevertheless, the actual measured strain can be adjusted to accurately determine the deformation of the soil by using this coefficient.

**FIG. 17**

Changes in  $DC_{f-s}$  coefficient of TOCs with increasing number of cycles under wet conditions.

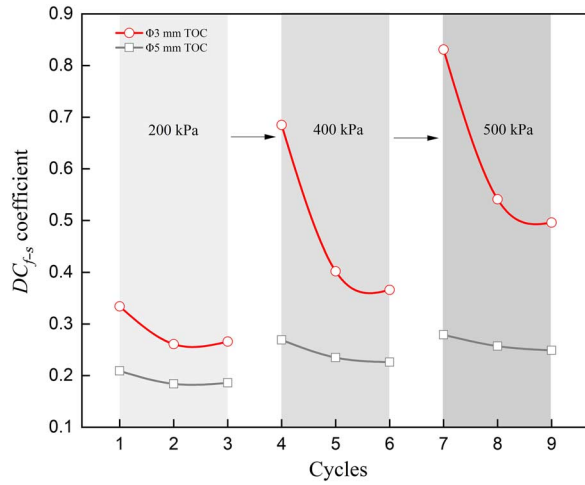


**Figure 17** illustrates the variation of  $DC_{f-s}$  coefficients with the loading–unloading cycles under wet conditions. The  $DC_{f-s}$  coefficients of TOCs is the biggest for the first cycle, followed by the second cycle, and the smallest for the third cycle under each confining pressure. The  $DC_{f-s}$  tends to be stable with the cycles under the same conditions. The  $DC_{f-s}$  coefficient of  $\Phi 3$  mm TOC is always larger than that of  $\Phi 5$  mm and the  $DC_{f-s}$  coefficients of both types of cables increase with the confining pressure.

## Discussion on the Relative Slippage between Cable Sheath and Sand

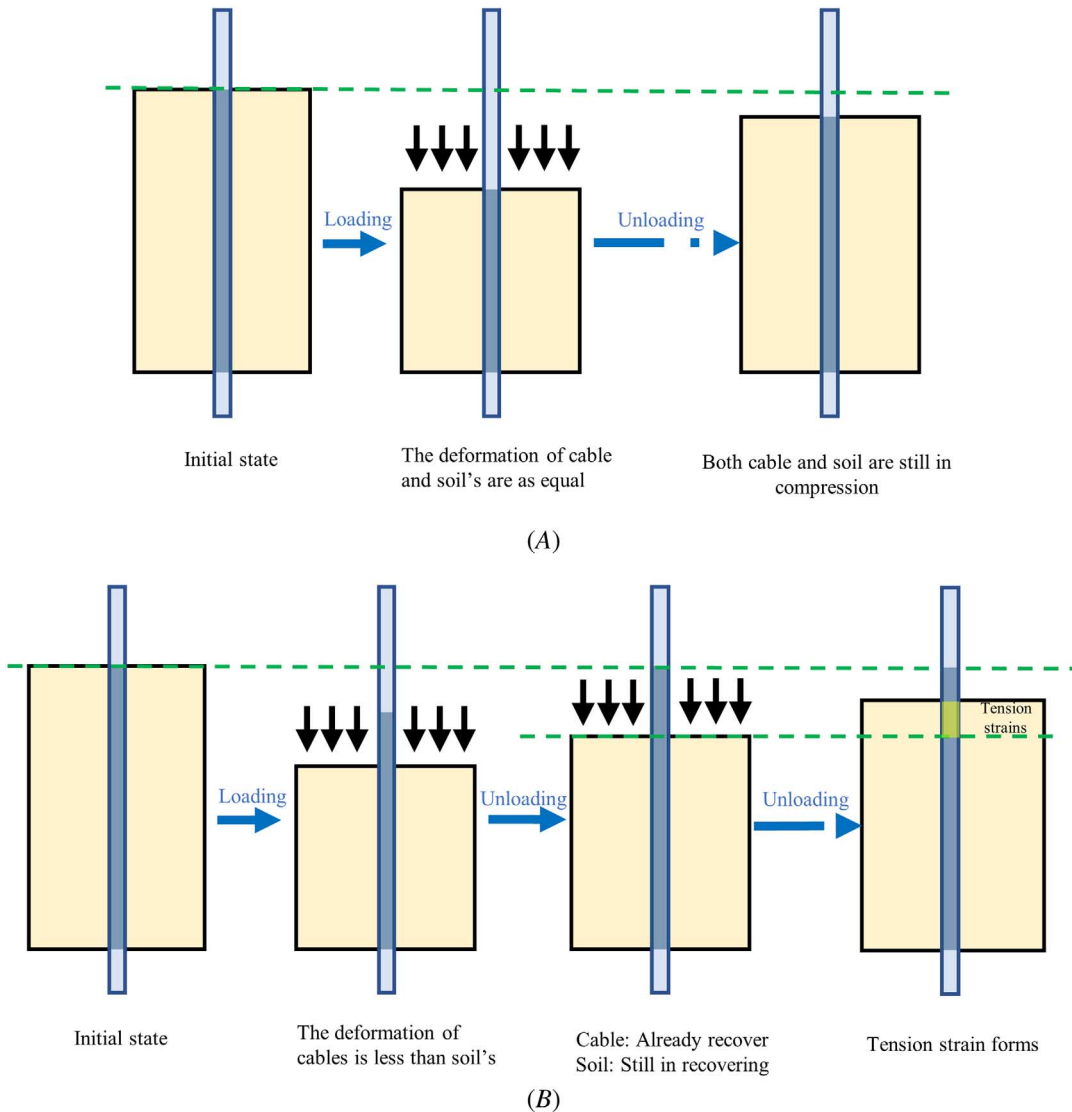
The specimen shows elastic-plastic behavior during loading and unloading. The optical sensing cable should always be in compression if there is no relative slippage between the optic cable and sand, as shown in **figure 18A**. The strain of the optical sensing fiber should remain compressive even after unloading. However, the tensile strains of the optical fiber can be seen at both ends and inside the specimen, as shown in **figure 19**. This tensile strain is common during unloading, and the tensile strain value is in the range of  $0 \mu\epsilon$  to  $-40 \mu\epsilon$ . Both optical cables and specimens are compressed during loading. However, the compressive strain of optical cable is smaller than that of the specimen because of relative slippage between the sheath and sand. The optical cable has higher modulus of elasticity, and its compressive deformation recovers faster than that of the sand specimen during unloading. As a result, the optical cable is stretched with the further rebound of the specimen, which results in small tensile strains in the optical fiber, as shown in **figure 18B**. The tensile strain of the optical fiber indirectly proves the relative slippage between cable sheath and sand.

## Conclusions

In this paper, a triaxial test method is proposed to study the deformation coordination between sand backfills and three types of optical cables ( $\Phi 3$  mm TOC,  $\Phi 5$  mm TOC, and  $\Phi 3$  mm LOC). Loading–unloading cycle tests were performed on specimens under confining pressures of 200 kPa, 400 kPa, and 500 kPa to analyze the influence of different optical cable structures on  $DC_{f-s}$ . The main conclusions are as follows.

- (1) The  $DC_{f-s}$  is influenced by the sheath structure of the optical cable, the number of loading–unloading cycles, and the level of the confining pressure in the soil.

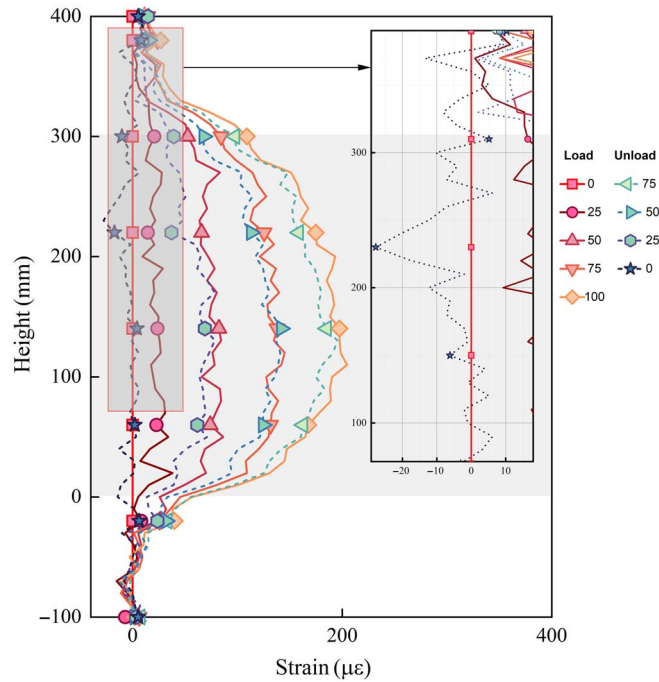
**FIG. 18** Schematic diagram of the tension strain: (A) the situation when relative slip never occurs and (B) the situation in which relative slip occurs.



- (2) The  $DC_{f-s}$  of LOC is poor because of the loose-tube structure. The sheath of  $\Phi 5$  mm TOC is thick and has a complex structure with built-in steel strands, which affects the strain transfer from the soil to the fiber and leads to a lower  $DC_{f-s}$ . In contrast, the sheath of  $\Phi 3$  mm TOC is thin and has a simpler structure, which enables better strain transfer. As a result, the  $\Phi 3$  mm TOC exhibits the best  $DC_{f-s}$  among the three cables.
- (3) The  $DC_{f-s}$  coefficient increases when the confining pressure was raised from 200 kPa to 500 kPa. A negative correlation between the  $DC_{f-s}$  coefficient and the loading–unloading cycles is observed. However, the  $DC_{f-s}$  coefficient rapidly tends to be constant as the number of loading–unloading cycles increases.
- (4) Although the relative slippage between the cable sheath and sand cannot be ignored, the  $DC_{f-s}$  coefficient can cover the effects of the slippage.

**FIG. 19**

Tensile strain in optical cables.



## Discussion

Deformation monitoring of soil plays an important role in the prevention and management of land subsidence. DFOS can be used for on-site deformation monitoring. Typically, an optical sensing cable is installed in a borehole and then the borehole is backfilled with sand or other geomaterials. The optical cable is in direct contact with the backfills. The strain transfer effect between the fiber and backfills is a crucial factor in the successful application of DFOS. The deformation of the soil is transmitted through the backfills to the optical fiber when land subsidence occurs. The land subsidence can be monitored by analyzing the fiber strain. However, the sensing performance of the optical cable is affected by various factors, such as the type of optical cable used and the stresses in soil. To further improve the accuracy of DFOS-based land subsidence monitoring, this study proposes conducting a simulation triaxial test on the optical sensing cable installed within the monitoring borehole. This test aims to obtain the  $DC_{f-s}$  coefficient to calibrate the fiber strain and improve the precision of the strain measurements.

The confining pressure applied in the triaxial test corresponds to the installation depth of the optical cable. The  $DC_{f-s}$  coefficient at different depth can be determined by applying relevant confining pressure in the triaxial test. Then, the strain distribution along the optical sensing cable in the land subsidence monitoring can be calibrated by the  $DC_{f-s}$  coefficient at the corresponding depth.

Fluctuation of the groundwater level leads to the changes of soil stress, which is equivalent to the loading–unloading process in the triaxial test. The  $DC_{f-s}$  coefficient tends to be stable with the loading–unloading cycles, based on which it can be deduced that the  $DC_{f-s}$  coefficient will converge to a constant value after multiple groundwater level fluctuations in the land subsidence monitoring.

Therefore, by conducting cyclic triaxial tests on the installed optical sensing cable and the backfills of the borehole under different confining pressures, a reliable distribution of the  $DC_{f-s}$  coefficient with the depth is obtained.

The application of strain sensing optical cables, characterized by a diversity of sheath structures, enhances their robustness in engineering monitoring. Selecting optical cables with appropriate structural types is crucial and should be based on specific on-site environmental conditions. This study acknowledges the variability in natural conditions, such as water content of soil, confining pressure, and cyclic loading across different sites. We introduce the  $DC_{f-s}$  coefficient, derived from the triaxial tests, as a pivotal correction factor. According to equation (26), the  $DC_{f-s}$  coefficient enables the refinement of strain data captured by on-site distributed optical fiber sensing systems, substantially increasing the monitoring precision of the soil deformation.

$$d_s = \frac{d_{TOC}}{DC_{f-s}} \quad (26)$$

where  $d_s$  represents the true deformation of soil and  $d_{TOC}$  represents deformation measured by TOCs.

The employment of this enhanced data allows for more accurate monitoring of urban ground deformation, thereby facilitating timely early warnings for ground subsidence and associated urban geohazards. Future research could focus on extending this approach to a wider range of soil types and environmental conditions, along with integrating advanced data analytics for a more nuanced interpretation of the monitoring data. Such advancements will contribute significantly to the fields of urban geotechnical monitoring and hazard mitigation.

## ACKNOWLEDGMENTS

This work was supported by the National Natural Science Foundation of China (No. 42077233) and the Natural Science Foundation of Jiangsu Province (BK20231409).

## References

- Amer, R., Z. Xue, T. Hashimoto, and T. Nagata. 2021. "Distributed Fiber Optic Strain Sensing for Geomechanical Monitoring: Insights from Field Measurements of Ground Surface Deformation." *Geosciences* 11, no. 7 (July): 285. <https://doi.org/10.3390/geosciences11070285>
- Ansari, F. and Y. Libo. 1998. "Mechanics of Bond and Interface Shear Transfer in Optical Fiber Sensors." *Journal of Engineering Mechanics* 124, no. 4 (April): 385–394. [https://doi.org/10.1061/\(ASCE\)0733-9399\(1998\)124:4\(385\)](https://doi.org/10.1061/(ASCE)0733-9399(1998)124:4(385))
- Bagheri-Gavkosh, M., S. M. Hosseini, B. Ataie-Ashtiani, Y. Sohani, H. Ebrahimian, F. Morovat, and S. Ashrafi. 2021. "Land Subsidence: A Global Challenge." *The Science of the Total Environment* 778: 146193. <https://doi.org/10.1016/j.scitotenv.2021.146193>
- Barrias, A., J. R. Casas, and S. Villalba. 2016. "A Review of Distributed Optical Fiber Sensors for Civil Engineering Applications." *Sensors* 16, no. 5 (May): 748. <https://doi.org/10.3390/s16050748>
- Calderhead, A. I., R. Therrien, A. Rivera, R. Martel, and J. Garfias. 2011. "Simulating Pumping-Induced Regional Land Subsidence with the Use of InSAR and Field Data in the Toluca Valley, Mexico." *Advances in Water Resources* 34, no. 1 (January): 83–97. <https://doi.org/10.1016/j.advwatres.2010.09.017>
- Chen, Y. and D. Zhang. "The Pullout Test to Study the Interface Effect between the Optical Sensing Fiber and the Soil." Master's thesis, Nanjing University, 2011. <http://dx.doi.org/10.2139/ssrn.4293178>
- Dehghani, M., M. J. Valadan Zoj, A. Hooper, R. F. Hanssen, I. Entezam, and S. Saatchi. 2013. "Hybrid Conventional and Persistent Scatterer SAR Interferometry for Land Subsidence Monitoring in the Tehran Basin, Iran." *ISPRS Journal of Photogrammetry and Remote Sensing* 79: 157–170. <https://doi.org/10.1016/j.isprsjprs.2013.02.012>
- Fan, H., K. Deng, C. Ju, C. Zhu, and J. Xue. 2011. "Land Subsidence Monitoring by D-InSAR Technique." *Mining Science and Technology (China)* 21, no. 6 (November): 869–872. <https://doi.org/10.1016/j.mstc.2011.05.030>
- Gao, J., B. Shi, W. Zhang, and H. Zhu. 2006. "Monitoring the Stress of the Post-tensioning Cable Using Fiber Optic Distributed Strain Sensor." *Measurement* 39, no. 5 (June): 420–428. <https://doi.org/10.1016/j.measurement.2005.12.002>
- Gu, K., B. Shi, C. Liu, H. Jiang, T. Li, and J. Wu. 2018. "Investigation of Land Subsidence with the Combination of Distributed Fiber Optic Sensing Techniques and Microstructure Analysis of Soils." *Engineering Geology* 240: 34–47. <https://doi.org/10.1016/j.enggeo.2018.04.004>
- Hasan, M. F., R. Smith, S. Vajedian, R. Pommerenke, and S. Majumdar. 2023. "Global Land Subsidence Mapping Reveals Widespread Loss of Aquifer Storage Capacity." *Nature Communications* 14, no. 1 (October): 6180. <https://doi.org/10.1038/s41467-023-41933-z>
- He, Y., G. Xu, H. Kaufmann, J. Wang, H. Ma, and T. Liu. 2021. "Integration of InSAR and LiDAR Technologies for a Detailed Urban Subsidence and Hazard Assessment in Shenzhen, China." *Remote Sensing* 13, no. 12 (June): 2366. <https://doi.org/10.3390/rs13122366>



- Kulpa, M., T. Howiacki, A. Wiater, T. Siwowski, and R. Sienko. 2021. "Strain and Displacement Measurement Based on Distributed Fibre Optic Sensing (DFOS) System Integrated with FRP Composite Sandwich Panel." *Measurement* 175: 109099. <https://doi.org/10.1016/j.measurement.2021.109099>
- Li, D., H. Li, L. Ren, and G. Song. 2006. "Strain Transferring Analysis of Fiber Bragg Grating Sensors." *Optical Engineering* 45, no. 2 (February): 024402. <https://doi.org/10.1117/1.2173659>
- Liang, Y., K. Gu, B. Shi, S. Liu, J. Wu, Y. Lu, and H. I. Inyang. 2022. "Estimation of Land Subsidence Potential via Distributed Fiber Optic Sensing." *Engineering Geology* 298: 106540. <https://doi.org/10.1016/j.enggeo.2022.106540>
- Liu, Y., T. Ma, and Y. Du. 2017. "Compaction of Muddy Sediment and Its Significance to Groundwater Chemistry." *Procedia Earth and Planetary Science* 17: 392–395. <https://doi.org/10.1016/j.proeps.2016.12.099>
- Liu, S.-P., B. Shi, K. Gu, C.-C. Zhang, J.-L. Yang, S. Zhang, and P. Yang. 2020. "Land Subsidence Monitoring in Sinking Coastal Areas Using Distributed Fiber Optic Sensing: A Case Study." *Natural Hazards* 103, no. 3 (September): 3043–3061. <https://doi.org/10.1007/s11069-020-04118-1>
- Sang, H., D. Zhang, Y. Gao, L. Zhang, G. Wang, B. Shi, B. Zheng, and Y. Liu. 2019. "Strain Distribution Based Geometric Models for Characterizing the Deformation of a Sliding Zone." *Engineering Geology* 263: 105300. <https://doi.org/10.1016/j.enggeo.2019.105300>
- Sasaki, T., S. Zhang, K. Soga, L. Luo, B. Freifeld, Y. Kitayama, K. Kawaguchi, and H. Sugiyama. 2021. "Distributed Fiber Optic Strain Sensing of Bending Deformation of a Well Mockup in the Laboratory." *Journal of Natural Gas Science and Engineering* 96: 104309. <https://doi.org/10.1016/j.jngse.2021.104309>
- Shi, B., D. Zhang, H. Zhu, C. Zhang, K. Gu, H. Sang, H. Han, M. Sun, and J. Liu. 2021. "DFOS Applications to Geo-engineering Monitoring." *Photonic Sensors* 11, no. 2 (June): 158–186. <https://doi.org/10.1007/s13320-021-0620-y>
- Sun, Y.-J., D. Zhang, B. Shi, H.-J. Tong, G.-Q. Wei, and X. Wang. 2014. "Distributed Acquisition, Characterization and Process Analysis of Multi-field Information in Slopes." *Engineering Geology* 182, Part A (November): 49–62. <https://doi.org/10.1016/j.enggeo.2014.08.025>
- Wang, H. Y., D. Zhang, K. Ren, B. Shi, J. Guo, and M. Sun. 2023. "The Sensing Performance of a Novel Optical Cable for Tunnel Water Leakage Monitoring Based on Distributed Strain Sensing." *IEEE Sensors Journal* 23, no. 19 (October): 22496–22506. <https://doi.org/10.1109/JSEN.2023.3295429>
- Wu, J., H. Jiang, J. Su, B. Shi, Y. Jiang, and K. Gu. 2015. "Application of Distributed Fiber Optic Sensing Technique in Land Subsidence Monitoring." *Journal of Civil Structural Health Monitoring* 5, no. 5 (November): 587–597. <https://doi.org/10.1007/s13349-015-0133-8>
- Wu, H., H.-H. Zhu, C.-C. Zhang, G.-Y. Zhou, B. Zhu, W. Zhang, and M. Azarafza. 2020. "Strain Integration-Based Soil Shear Displacement Measurement Using High-Resolution Strain Sensing Technology." *Measurement* 166: 108210. <https://doi.org/10.1016/j.measurement.2020.108210>
- Wu, J., B. Shi, K. Gu, S. Liu, and G. Wei. 2021. "Evaluation of Land Subsidence Potential by Linking Subsurface Deformation to Microstructure Characteristics in Suzhou, China." *Bulletin of Engineering Geology and the Environment* 80, no. 3 (March): 2587–2600. <https://doi.org/10.1007/s10064-020-02056-7>
- Wu, G.-Z., D. Zhang, T.-S. Shan, B. Shi, Y.-J. Fang, and K. Ren. 2022. "Characterizing the Strain Transfer on the Sensing Cable-Soil Interface Based on Triaxial Testing." *Smart Structures and Systems* 30, no. 1 (July): 63–74. <https://doi.org/10.12989/sss.2022.30.1.063>
- Zhang, L., B. Shi, X. Zheng, and Y.-J. Sun. 2020. "DFOS-Based Association Rules Analysis on the Multi-fields Information of Majiagou Landslide." *IOP Conference Series: Earth and Environmental Science* 570, no. 4 (November): 042023. <https://doi.org/10.1088/1755-1315/570/4/042023>
- Zhang, C.-C., H.-H. Zhu, J.-K. She, D. Zhang, and B. Shi. 2015. "Quantitative Evaluation of Optical Fiber/Soil Interfacial Behavior and Its Implications for Sensing Fiber Selection." *IEEE Sensors Journal* 15, no. 5 (May): 3059–3067. <https://doi.org/10.1109/JSEN.2014.2386881>